# Experimental investigation of the initial-state alignment dependence in the energy pooling process: $Ca(4s4p\ ^3P_1)+Ca(4s4p\ ^3P_1)\rightarrow Ca(4s4p\ ^1P_1)+Ca(4s^2)$

Harold V. Parks, Eileen M. Spain,* John E. Smedley,† and Stephen R. Leone
*JILA, National Institute of Standards and Technology and University of Colorado, Department of Physics, University of Colorado, Boulder, Colorado 80309-0440*
(Received 11 March 1998)

A pulsed laser investigation is performed to study the detailed effects of electronic angular-momentum alignment on the cross section for the energy-transfer process $Ca(4s4p\ ^3P_1)+Ca(4s4p\ ^3P_1)\rightarrow Ca(4s4p\ ^1P_1)+Ca(4s^2)$. A uniform magnetic field imposed by a set of Helmholtz coils is used to systematically precess the initial state orbitals with a well-defined period, allowing different alignments to be sampled at different time delays after the pulsed laser excites and aligns the $Ca(4s4p\ ^3P_1)$ states. The polarization effects in this collision process are striking. For example, the cross section for two atoms both in the $m_j=0$ magnetic substrate is 13 times larger than the cross section for two atoms that are both in the $m_j=1$ (or $-1$) substrate, where the quantization axis is taken to be along the relative velocity vector of the collision. The initial *m*-sublevel dependence of this three-vector correlation process can be completely described with eight fundamental parameters, five of which are accurately obtained. In addition, the coarse energy dependence of these parameters is deduced. [S1050-2947(98)08909-4]

PACS number(s): 34.50.Pi, 34.50.Rk

## I. INTRODUCTION

Measurement of the effects of orbital alignment and orientation on atomic collisions provides rigorous details about the *m*-sublevel dependence of the collision dynamics [1–4]. The results of these measurements address more detailed information about the potential-energy surfaces of the system and relevant curve crossings, as well as exacting tests of collision theory. Most frequently the measurements are two-vector correlation experiments, meaning that the alignment of an excited atom (the first vector) is defined with respect to the relative velocity vector of the collision (the second vector) [5–7]. In other experiments three-vector correlations were studied, including either initial and final alignments of the atomic orbitals plus the relative velocity vector [8,9] or initial and final relative velocities together with one atomic alignment [10]. Four-vector correlation experiments have been done involving the initial and final velocity together with initial and final alignments [11]. Another three-vector correlation involves two initial orbitals aligned with respect to the relative velocity vector of the collision. An excellent example of this type of experiment was performed on the $Na(3p)+Na(3p)$ associative ionization process [12–14]. Similar experiments have been done for $Na(3p)+Na(3p)$ energy pooling [15].

In this paper we investigate the effects of the alignment of the initial states on the energy pooling process

$$Ca(4s4p\ ^3P_1)+Ca(4s4p\ ^3P_1)\rightarrow Ca(4s4p\ ^1P_1)+Ca(4s^2). \quad (1)$$

In addition to Na, energy pooling has been studied extensively in alkaline-earth metals: Gallagher and co-workers studied energy pooling from the low-lying states of Sr [16,17] and Neuman, Gallagher, and Cooper studied this process [Eq. (1)] in Ba [18]. Neuman and Gallagher have also reported a preliminary alignment study for Sr energy pooling [19]. In the present work we extract considerably more alignment information than Gallagher and co-workers' technique allows. Energy pooling with Ca has been observed in gas cells [20,21] and the process in Eq. (1) was observed by Husain and Roberts [21]. The pooling process in Eq. (1) is unusual in that 6768 $cm^{-1}$ of electronic energy must be converted into kinetic energy. It has been thought that such very exothermic processes would be very unlikely; however, a similar highly exothermic energy pooling process has recently been observed in Sr [17].

The energy pooling in Eq. (1) may be an ideal system for studying spin-orbit coupling in collisions between aligned atoms, an effect that has not be explored in other studies such as those on Na energy pooling [22]. Since the collision time is nearly an order of magnitude longer than the spin-orbit precession rate, the spin-orbit interaction should have a large influence on the collision cross sections. Also, since we excite to a $j=1$ state of Ca, only eight cross-section parameters are needed to completely describe the alignment effects, as demonstrated in Sec. II. This makes Eq. (1) particularly simple to study. In addition, the total energy of the system in Eq. (1) is low enough so that only a relatively limited number of molecular states are involved, which should eventually permit theoretical approaches to interpret the results.

We use a method of controlling the orbital alignment that employs magnetic precession. Meijer *et al.* used a similar technique with cw lasers to study associative ionization in Na [23]. In our experiment, the use of pulsed lasers to excite the long-lived $Ca(4s4p\ ^3P_1)$ state is a considerable simpli-

*Present address: Department of Chemistry, Occidental College, Los Angeles, CA 90041.
†Present address: Department of Physics and Astronomy, Bates College, Lewiston, ME 04240.

 

fication. Here all of the excited atoms initially have the same angular-momentum alignment, determined by the polarization of the excitation laser. Then all the atoms precess at the same rate. This experiment is done in a single effusive beam and the final Ca($4s4p\ ^1P_1$) state is detected by fluorescence as it decays to the ground state.

In Sec. II of this paper we define the fundamental cross sections needed to describe energy pooling between two identical $j=1$ orbitals. The exact form of the experimentally observed cross sections is derived in terms of these fundamental parameters. In Sec. III we describe the details of the experimental apparatus. Section IV considers the results and Sec. V presents a discussion and conclusion. We find that there are very pronounced polarization effects. There is enough time for the alignment to be significantly altered as the atoms make the transition from separated, noninteracting atoms to a molecular complex, but the asymptotic initial polarization still has a large effect on the outcome of the collision. Alternative theoretical techniques may be needed to describe the higher-order alignment effects.

## II. THEORETICAL BACKGROUND

We introduce a set of fundamental cross sections to quantitatively describe the observed alignment effects for the specific case of a three-vector correlation involving two excited atomic states colliding. The values $m_1$ and $m_2$ are the $m_j$ magnetic quantum numbers of the initial states of each of the colliding ($^3P_1$) atoms, respectively. The quantization axis lies along the relative velocity vector of the collision; in this case this collision frame is the axis of the single effusive beam. The product state of the energy pooling collision is observed when it fluoresces. This signal is proportional to the total cross section for energy pooling, which can be written [24]

$$\sigma_{\text{expt}}=\sum_{m_1,m_1',m_2,m_2'}\rho_{m_1m_1'}\rho_{m_2m_2'}\sigma_{m_1m_2;m_1'm_2'}, \tag{2}$$

where $\rho_{m_1m_1'}$ and $\rho_{m_2m_2'}$ are the density matrices describing the states of each of the colliding atoms. The $\sigma_{m_1m_2;m_1'm_2'}$ are the fundamental cross sections defined by

$$\sigma_{m_1m_2;m_1'm_2'}=\int f_{m_1m_2}(\theta,\varphi)f^*_{m_1'm_2'}(\theta,\varphi)d\Omega. \tag{3}$$

Here $f_{m_1m_2}$ represents the scattering amplitude for an atom in a state $m_1$ to undergo an energy pooling process upon collision with an atom in state $m_2$. We measure only total cross sections in this experiment, so the integration is over all scattering angles. These cross sections have also been implicitly integrated over some initial kinetic-energy distribution (which will be addressed later). In addition, the possibility of final-state alignment is neglected, but it will be the subject of future work [25].

There are two types of fundamental cross sections. If $m_1'=m_1$ and $m_2'=m_2$ in Eq. (3), then here the cross section is termed a conventional cross section. We will denote these cross sections by $\sigma_{m_1m_2}$. Conventional cross sections have real positive values. For instance, $\sigma_{m_1m_2}$ is the cross section for an energy pooling collision between an atom in state $m_1$ and an atom in state $m_2$. In the second type of cross section, termed coherence cross sections, $m_1$ and $m_2$ are not equal to $m_1'$ and $m_2'$ in Eq. (3). The coherence cross section $\sigma_{m_1m_2;m_1'm_2'}$ describes how the interference between two channels contributes to the experimentally observed cross sections. For example, the system may be in a superposition of two states, one with colliding atoms in the $m_1$ and $m_2$ magnetic sublevels and the other with the atoms in the $m_1'$ and $m_2'$ magnetic sublevels. Then $\sigma_{m_1m_2;m_1'm_2'}$ represents the interference term between the amplitudes for pooling from each of the two states. In general, coherence cross sections are complex valued.

The number of fundamental cross sections that contribute to the experimentally measured cross section represented by Eq. (2) is quite large, 81 for this experiment. However, most of these cross sections are not independent of each other. The number of independent parameters needed to describe the collision process is reduced by symmetry considerations. First, it can immediately be seen from Eq. (3) that

$$\sigma_{m_1m_2;m_1'm_2'}=\sigma^*_{m_1'm_2';m_1m_2}. \tag{4}$$

Since the cross sections should be invariant under a frame inversion,

$$\sigma_{m_1m_2;m_1'm_2'}=\sigma_{-m_1-m_2;-m_1'-m_2'}. \tag{5}$$

Then, by using Eq. (3) and the Schwarz inequality it can be shown that

$$|\sigma_{m_1m_2;m_1'm_2'}|\leqslant\sigma_{m_1m_2}\sigma_{m_1'm_2'}; \tag{6}$$

Further, since we have chosen the relative velocity vector to lie along the quantization axis, the initial orbital angular momentum has no component along this axis. Therefore, the total **z** component of angular momentum of the system is $M=m_1+m_2$. Since there is no coupling between channels with different $M$,

$$\sigma_{m_1m_2;m_1'm_2'}=0 \quad \text{unless} \quad m_1+m_2=m_1'+m_2'. \tag{7}$$

In addition, since we are colliding Ca with Ca we have

$$\sigma_{m_1m_2;m_1'm_2'}=\sigma_{m_2m_1;m_2'm_1'}. \tag{8}$$

Using Eqs. (4) and (8), both $\sigma_{10:01}$ and $\sigma_{1-1:-11}$ must be real. Using Eqs. (4), (5), (7), and (8), we find that the number of independent parameters on the right-hand side of Eq. (2), which determines the total experimental cross section, is reduced to eight: four conventional cross sections, two entirely real coherence cross sections, and the real and imaginary parts of one other coherence cross section. These parameters are

$$\sigma_{00},\ \sigma_{10},\ \sigma_{1-1},\ \sigma_{11},\ \sigma_{01;10},\ \sigma_{1-1;-11},$$
$$\text{Re}(\sigma_{00;1-1}),\ \text{Im}(\sigma_{00;1-1}). \tag{9}$$

We now show how the signals that are actually measured in the laboratory can be expressed in terms of the fun-

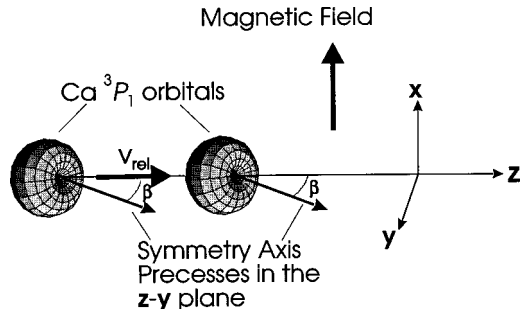


FIG. 1. Schematic of the Ca($4s4p\ ^3P_1$) orbitals in the atomic beam. The shape for each orbital shown here represents the angular distribution of the electron density. The relative velocity of the collision $\mathbf{v}_{rel}$ lies along the **z** axis. This causes the symmetry axis of the orbitals to precess around the direction of the magnetic field, which is parallel to the **x** axis. The angle between the symmetry axis and the **z** axis is $\beta$.

damental cross sections listed in Eq. (9). The experiment is performed with a combination of linearly polarized laser excitation and magnetic-field precession techniques. Fluorescence is detected from either the final state or the initially populated state. If we excite Ca from the ground *s* state to a *p* state with a linearly polarized laser, a pure $m_j=0$ excited state is produced if the polarization is parallel to the quantization axis (Fig. 1). We define the symmetry axis of the orbital to be the quantization axis that, at any instant, gives a pure $m_j=0$ state. Immediately after the excitation laser pulse, the symmetry axis and the laser polarization point in the same direction, but at later times the applied magnetic field causes the symmetry axis to precess. To express the energy pooling cross section for this orbital in terms of the fundamental cross sections we transform from the frame of quantization along the symmetry axis back to the collision. This is done by applying the appropriate rotation operator to the density matrix of the pure $m_j=0$ state. If the angle between the symmetry axis and the relative velocity vector of the collision is defined to be $\beta$, the new density matrix is a function of $\beta$. All of the atoms in this experiment are excited with the same laser, so each collision involves two atoms with the same orbital alignment. Upon inserting the density matrix for both atoms into Eq. (2) an expression is obtained for the total cross section or signal intensity for energy pooling in terms of the fundamental cross sections as a function of $\beta$:

$$I_l(\beta)=\frac{n}{8}[(4\sigma_{00}-2\sigma_{11}-2\sigma_{1-1}-2\sigma_{1-1;-11})\cos 2\beta + (\sigma_{00}+\tfrac{1}{2}\sigma_{11}+\tfrac{1}{2}\sigma_{1-1}+\tfrac{1}{2}\sigma_{1-1;-11}-2\sigma_{01}-2\sigma_{01;10} + 2\ \mathrm{Re}\ \sigma_{00;1-1})\cos 4\beta+(3\sigma_{00}+\tfrac{3}{2}\sigma_{11}+\tfrac{3}{2}\sigma_{1-1} + \tfrac{3}{2}\sigma_{1-1;-11}+2\sigma_{01}+2\sigma_{01;10}-2\ \mathrm{Re}\ \sigma_{00,1-1})], \tag{10}$$

where the subscript *l* refers to the linearly polarized excitation and *n* is a normalization constant that relates the cross sections to the actual signal intensity.

We can also excite the orbital with circularly polarized light instead of linearly polarized light. In this case, if the symmetry vector lies along the direction of laser propagation, a pure $m_j=1$ state results immediately after the laser pulse. We could equally well have defined the symmetry vector so that a pure $m_j=-1$ state results [see Eq. (5)].

As in the case of linear polarization, transformation to the collision frame with the appropriate rotation matrices for these $m_j=1$ states gives

$$I_c(\beta)=\frac{n}{8}[(-\sigma_{00}+\tfrac{28}{8}\sigma_{11}-\tfrac{1}{2}\sigma_{1-1}-\tfrac{1}{2}\sigma_{1-1;-11}-2\sigma_{10} - 2\sigma_{01;10}-2\ \mathrm{Re}\ \sigma_{00;1-1})\cos 2\beta+(\tfrac{1}{4}\sigma_{00}+\tfrac{1}{8}\sigma_{11} + \tfrac{1}{8}\sigma_{1-1}+\tfrac{1}{8}\sigma_{1-1;-11}-\tfrac{1}{2}\sigma_{01}-\tfrac{1}{2}\sigma_{01;10} + \tfrac{1}{2}\ \mathrm{Re}\ \sigma_{00;1-1})\cos 4\beta+(\tfrac{3}{4}\sigma_{00}+\tfrac{35}{8}\sigma_{11}+\tfrac{3}{8}\sigma_{1-1} + \tfrac{3}{8}\sigma_{1-1;-11}+\tfrac{5}{2}\sigma_{01}+\tfrac{5}{2}\sigma_{01;10}+\tfrac{3}{2}\ \mathrm{Re}\ \sigma_{00;1-1})], \tag{11}$$

where the subscript *c* refers to circularly polarized excitation. Thus the energy pooling signals are a function of $\beta$ and the fundamental cross sections; for both the linear and circular polarization cases, the form is

$$I(\beta)=a\ \cos(2\beta)+b\ \cos(4\beta)+c. \tag{12}$$

The constants *a*, *b*, and *c* are different for the linear and circular cases and are distinguished below by a subscript *l* for linear and *c* for circular. In this experiment, a pulsed laser with linear polarization prepares an orbital with $\beta=0°$ and circular polarization prepares an orbital with $\beta=90°$. The orbitals then precess in an applied magnetic field that is directed perpendicular to the symmetry axis. Since the angle by which the orbital precesses $\beta$ is directly proportional to the time after the laser pulse *t*, Eq. (12) can be rewritten

$$I(t)=a\ \cos[2(\omega t+\beta_0)]+b\ \cos[4(\omega t+\beta_0)]+c, \tag{13}$$

where $\omega$ is the precession frequency

$$\omega=\mu_B g B/\hbar. \tag{14}$$

Here *B* is the magnetic-field strength, $\mu_B$ is the Bohr magneton, and *g* is the Landé *g* factor, $\frac{3}{2}$ for the Ca($4s4p\ ^3P_1$) excited state studied in this experiment. Thus the energy pooling cross section or signal oscillates in time, with the amplitude of the oscillations given by the coefficients *a*, *b*, and *c* of Eq. (12), which depend on the fundamental cross sections listed in Eq. (9). Note that once an energy pooling process has occurred in this experiment, the product state radiatively decays with a mean lifetime of 4 ns. Thus, compared with the magnetic precession period of 0.8 $\mu$s used here, the fluorescence is observed instantaneously after the collision.

In this experiment, we do not measure the absolute values of $a_l$, $b_l$, $c_l$, $a_c$, $b_c$, and $c_c$. Rather, their relative values are obtained, which are defined below and denoted with primes:

$$a_l'=a_l/c_l,\quad b_l'=b_l/c_l,\quad a_c'=a_c/c_c,\quad b_c'=b_c/c_c. \tag{15}$$

We can also measure the ratio of intensities of the linear and circular polarization cases. This gives one more measured parameter, the ratio of the linear to circular signals at $\beta = 90°$:

$$r = \frac{I_l(\beta=90°)}{I_c(\beta=90°)} = \frac{-a_l+b_l+c_l}{-a_c+b_c+c_c}. \tag{16}$$

We can now solve Eqs. (10) and (11) for the fundamental cross sections, listed in Eq. (9), in terms of the parameters in Eqs. (15) and (16). The measured quantities are not all linearly independent. In order for a solution to exist the relation

$$b_l' = 4r\alpha b_c' \tag{17}$$

is required, where

$$\alpha \equiv \frac{-a_c'+b_c'+1}{-a_l'+b_l'+1}. \tag{18}$$

We take $b$ to be the average of the measured values of $b_c'$ and $b_l'/4r\alpha$ and obtain

$$\begin{aligned}
\sigma_{01}+\sigma_{01;10} &= -r\alpha a_c' - 7r\alpha b + r\alpha, \\
\text{Re}\ \sigma_{00;1-1} &= -r\alpha a_c' + 5r\alpha b + r\alpha, \\
\sigma_{00} &= a_l' + 4r\alpha b + 1, \\
\sigma_{11} &= r\alpha a_c' + r\alpha b + r\alpha, \\
\sigma_{1-1;-11}+\sigma_{1-1} &= -r\alpha a_c' - 2a_l' + 7r\alpha b - r\alpha + 2.
\end{aligned} \tag{19}$$

The normalization constant $n$ in Eqs. (10) and (11) has been arbitrarily set so that the signal with linear polarization when averaged over $\beta$ is equal to 1. Notice that one can get the sums $\sigma_{1-1}+\sigma_{1-1;-11}$ and $\sigma_{01}+\sigma_{01;10}$, but not all four parameters individually. Also, $\text{Im}(\sigma_{00;1-1})$ does not appear at all.

The fundamental cross sections may also be a function of the initial kinetic energy of the collision. The results obtained in this experiment, which is carried out in a single effusive atomic beam, represent the derived fundamental cross sections averaged over an energy distribution. Immediately after the laser pulse, the energy distribution of the collisions is equal to the relative kinetic-energy distribution within the atomic beam. However, as time progresses, high-energy collisions become less and less likely. This is because only a finite volume of atoms is excited. At late times most of the fast moving atoms in the excitation region will have passed most of the slow moving atoms, so there is little possibility of further collisions that involve a high relative velocity. This experiment cannot determine the precise energy dependence of the cross sections, but, as will be seen in Sec. IV, it is possible to quantitatively estimate how the velocity distribution and the cross sections vary with time. The signal that is observed at a particular alignment $d$ as a function of time is then related to the cross section as a function of velocity by

$$I_d(t) = \int_0^\infty v\,\sigma_d(v)\,g(v,t)\,dv, \tag{20}$$

where the density of colliding pairs with relative velocities between $v$ and $v+dv$ at time $t$, $g(v)$, is given by

$$g(v) = \int_0^\infty v\,h(v,u,t)\,f(u)\,f(u+v)\,du, \tag{21}$$

where $f(u)$ is the velocity distribution in the beam and $h(v,u,t)$ is described below. If $M$ is the mass of a Ca atom, $T$ is the temperature of the nozzle that produces the effusive atomic beam, and $k$ is the Boltzmann constant then

$$f(u) = \frac{4}{\sqrt{\pi}}\left(\frac{M}{2kT}\right)u^2 e^{-Mu^2/2kT}. \tag{22}$$

The function $h(v,u,t)$ in Eq. (21) depends on the geometry of the experiment. If we were able to observe all collisions in the beam and the initially excited region has length $s$ in the beam direction, then $h(v,u,t)$ is $(s-vt)\theta(v-s/t)$, where $\theta(x)$ is a step function. However, only collisions in a small region of the beam are detected. This introduces an additional factor. If the atoms are observed only until they have moved a distance $l$ down stream from the center of the excitation region then

$$h(v,u,t) = \begin{cases} s = vt, & u < \dfrac{l-s/2}{t} \\ (s-vt) - \left(\dfrac{s}{2}+ut-l\right), & \dfrac{l-s/2}{t} < u < \dfrac{l+s/2}{t} \\ 0, & u > \dfrac{l+s/2}{t}. \end{cases} \tag{23}$$

The geometry of this experiment can be reasonably well modeled by taking $s$ to be 3 mm (the width of the laser beam) and $l$ to be 7.5 mm. In reality, this is not perfect because the laser beam may have brightness variations across its width and the observation region does not have a perfectly abrupt cutoff.

The result is that the signal at any particular time is proportional to the weighted average of $\sigma(v)$ and the mean and width of the weighting distribution decrease with time. At $t = 0$ this distribution is just the velocity distribution of the beam, with a mean of 750 m/s and a full width at half maximum (FWHM) of 800 m/s. At later times, this distribution can be estimated from Eq. (20). At $t = 8\ \mu$s the mean falls to about 190 m/s and the FWHM is 210 m/s.

This variation in the energy distribution is much slower than the oscillations due to the precession of the atoms given by Eq. (12), which have a period of about 0.4 $\mu$s. Thus we can fit the cross section expression to each individual precession period. The slow variation of these fit parameters over time gives an indication of the dependence of the fundamental cross sections as a function of velocity.

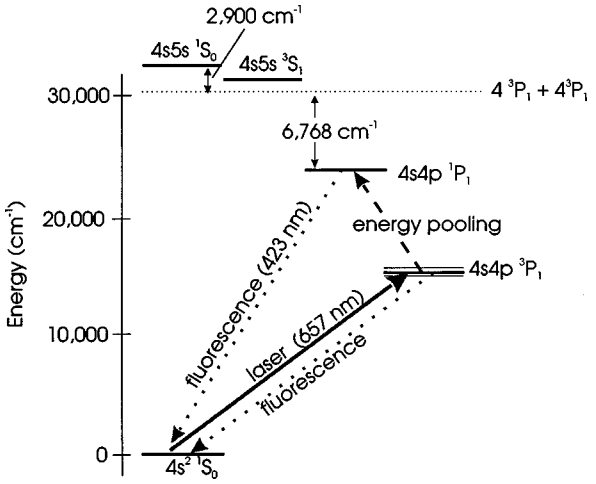


FIG. 2. Energy-level diagram showing the relevant Ca energy levels for this experiment. The dye laser, tuned to 657 nm, excites Ca in an atomic beam from the ground state to the Ca($4s4p\ ^3P_1$) level. We observe both the fluorescence from this initial state to the ground state and the 423-nm fluorescence from the Ca($4s4p\ ^1P_1$) energy level, which is populated by energy pooling collisions between two excited-state Ca atoms, shown by the dotted lines. Energy pooling to this $4s4p\ ^1P_1$ final state is exothermic since it lies 6768 $cm^{-1}$ below the total energy of the two initial $4s4p\ ^3P_1$ states.

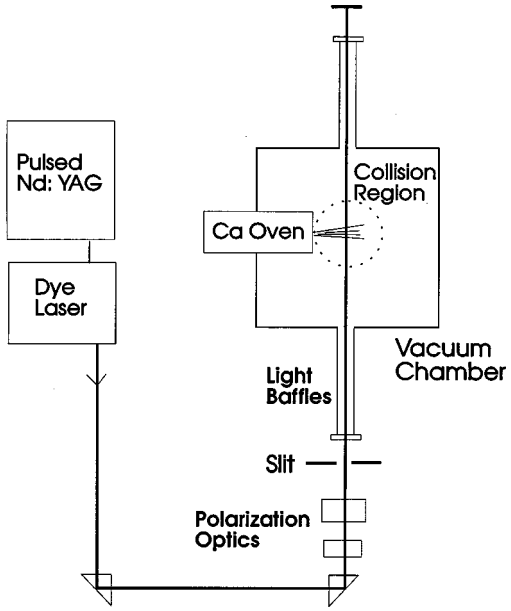


FIG. 3. Schematic of the experimental apparatus. Ground-state Ca atoms in an atomic beam are excited to the Ca($4s4p\ ^3P_1$) state with a pulsed Nd:YAG-pumped dye laser. The polarization of the laser is controlled by various optical components. The laser beam then passes through a 3-mm slit before entering the light baffles on the chamber.

## III. EXPERIMENTAL SETUP

In this experiment the effects of initial orbital alignment are studied for the process

$$\mathrm{Ca}(4s4p\ ^3P_1)+\mathrm{Ca}(4s4p\ ^3P_1)\rightarrow \mathrm{Ca}(4s4p\ ^1P_1)+\mathrm{Ca}(4s^2).$$

A pulsed dye laser excites ground-state Ca atoms into the initial $4s4p\ ^3P_1$ states in a single atomic beam. The alignment of the initial states immediately after the laser pulse is controlled by the polarization of this laser and the direction of the relative velocity vector is defined by the atomic beam axis. A magnetic field imposed by a set of Helmholtz coils causes the initial-state orbitals to precess with a well-defined period so that different alignments at different time delays after the laser pulse are sampled. Fluorescence is detected from the final $4s4p\ ^1P_1$ state produced by energy pooling. Compared to the precession period of the initial states, about 0.8 $\mu$s, the lifetime of the final state is very short, about 4 ns. Thus, by measuring the amount of final-state fluorescence as a function of time, the energy pooling cross section is mapped versus the rotation of the orbitals. By using both linear and circular laser polarization and carefully choosing the magnetic precession direction, most of the fundamental cross sections can be extracted. Since the highest relative velocity collisions only occur at the earliest times, the change in the cross-section parameters over several precession periods permits the approximate collision energy dependence of these parameters to be obtained.

The relevant Ca energy levels for this experiment are shown in Fig. 2. The dye laser, tuned to 657 nm, excites Ca in an atomic beam from the ground state to the Ca($4s4p\ ^3P_1$) level. Collisions between two of these excited atoms can result in energy pooling to the $4s4p\ ^1P_1$ state. Fluorescence is detected from the initial $4s4p\ ^3P_1$ state at 657 nm and the final $4s4p\ ^1P_1$ state at 423 nm. Since the $4s4p\ ^1P_1$ state lies 6768 $cm^{-1}$ below the total energy of the two initial $4s4p\ ^3P_1$ states, the excess energy is transformed into kinetic energy. Energy pooling to either the $4s5s\ ^1S_0$ or the $4s5s\ ^3S_1$ levels can also occur, although these processes are slightly endothermic. The possibility of energy pooling to the $4s5s\ ^1S_0$ state is particularly significant since any atoms in the $4s5s\ ^1S_0$ state will decay by emission through the $4s4p\ ^1P_1$ state and thus contribute to the 423-nm fluorescence signal. However, within 2 $\mu$s after the laser pulse all of the potential collisions in the observation zone with sufficient relative kinetic energy to reach this $4s5s\ ^1S_0$ state will have occurred. Thus the measurement of the 423-nm fluorescence is delayed to eliminate this possible interference.

The apparatus used for this experiment is shown in Fig. 3. A Nd:YAG (where YAG denotes yttrium aluminum garnet) pumped pulsed dye laser is tuned to 657 nm and has a frequency resolution of 0.05 $cm^{-1}$. This laser excites the ground-state Ca atoms in the atomic beam to the Ca($4s4p\ ^3P_1$) state. The laser pulse has a full width half maximum of 5 ns and a 10-Hz repetition rate. The pulse energies are typically 1–2 $mJ/cm^2$. This energy is sufficient to nearly saturate the transition from the ground state to the $4s4p\ ^3P_1$ state. Before this beam enters the chamber, it is manipulated by one or more polarization optics. The exact setup of these optics depends on the polarization needed. If linear, vertical polarization is needed; the light, which is already polarized mostly in the vertical direction, is simply passed through a Glan-Taylor prism to clean up the polarization. If horizontal polarization is required, the laser first passes through a double Fresnel rhomb to rotate the polar-

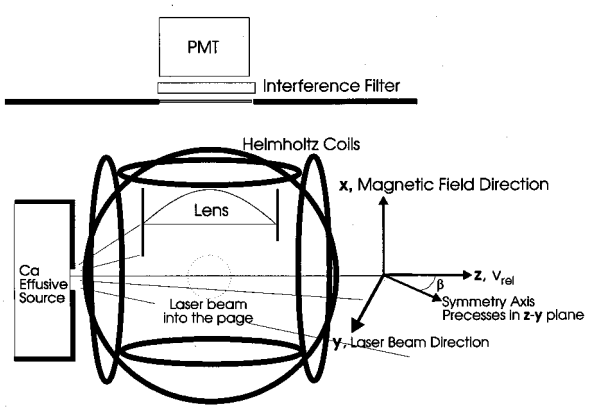


FIG. 4. Closeup view of the interaction region. The effusive source for the Ca beam is an oven held at a temperature of 975 K. An aspheric lens focuses the Ca fluorescence onto the cathode of a PMT. No skimmer is used for the Ca beam, but a shield is placed around the front of the lens to keep Ca from depositing on the surface of the lens. An interference filter is placed in front of the PMT to select either the 423-nm fluorescence from the final state or the 657-nm fluorescence from the initial state. Three orthogonal sets of Helmholtz coils are placed around the interaction region to control the magnetic field. In all of the experiments described in this paper, the magnetic field points along either the **x** or the **z** axis. The **z** axis is defined to lie in the direction of the Ca beam propagation, the **x** axis points from the collision region to the lens, and the **y** axis is parallel to the laser-beam propagation pointing into the page.

ization before passing through the Glan-Taylor prism. If circular polarization is needed, the laser runs through a Glan-Taylor prism and then a $\frac{1}{4}$-wave plate. Finally, just before entering the chamber, the laser light passes through a vertical slit with a width of 3 mm to produce a well-defined excitation zone perpendicular to the direction of the Ca beam.

Figure 4 shows a closeup of the interaction region. The effusive source for the Ca beam is an oven at 975 K. The nozzle, which has a 1 mm $\times$ 2 mm (horizontal) opening, is heated to a slightly higher temperature, 1020 K, to minimize clogging. At this temperature, the average collision velocity within the beam is 800 m/s. The Ca density in the collision region, which is 6 cm from the nozzle, is at most $8 \times 10^{10}$ atoms/cm$^3$ (much of the time it is lower than this, since Ca tends to partially clog the nozzle). The background pressure in the main vacuum chamber is typically $3 \times 10^{-5}$ Pa ($2 \times 10^{-7}$ Torr) while the oven is operating. Even if the summed cross section for all possible state changing collisions is taken to be very large, 100 Å$^2$, the probability for collision between any two atoms (excited or unexcited) is 0.001 over the time duration (10 $\mu$s) of this experiment. Thus single-collision conditions are obeyed.

The coordinate system used in our analysis is also shown in Fig. 4. The **z** direction is defined to lie along the direction of the Ca beam propagation, which is also the direction of the average relative velocity vector. The **x** axis points from the collision region to the lens. The applied magnetic field points along this axis. The **y** axis is parallel to the laser-beam propagation and points out of the page in Fig. 4.

The region from which the fluorescence can be collected is bounded in the **x** direction by the height of the laser beam, usually about 8 mm, and in the **yz** plane by the area imaged by the lens. This aspheric lens, shown in Fig. 4, has a focal length of 3.5 cm and a diameter of 5.0 cm. It is placed so that the center of the collision region is 2 cm below the plano face of the lens. This gives a region approximately 1 cm in diameter that is imaged onto the photomultiplier. To keep Ca from depositing on the surface of the lens a shield is placed around it as shown. An interference filter is placed in front of the photomultiplier tube (PMT) to select either the 423-nm fluorescence from the final state or the 657-nm fluorescence from the initial state. The transmission peak of the filter for the 423-nm line is centered at 420 nm and for the 657-nm line the filter is centered at 660 nm. Both interference filters have a FWHM transmission of 10 nm.

Also shown in Fig. 4 are the three orthogonal sets of Helmholtz coils used to control the magnetic field in the interaction region. In all of the experiments described in this paper, the magnetic precession field points along either the **x** or the **z** axis. Each coil has a diameter of about 25 cm and a separation of 12 cm. Each coil has seven windings, so that a current of about 1 A in each pair produces a magnetic field of 0.2 G, which causes the initial state orbitals to precess at approximately 1 MHz. The current in these coils is set by first nulling out the background field. This is done by adjusting the current in the coils until the modulation in the initial-state fluorescence due to precession has a period greater than 20 $\mu$s (the longest precession rate that we can observe). An additional current is then added to (or subtracted from) the appropriate coil to direct the magnetic field along either the **x** or the **z** axis.

The $4s4p\ ^3P_1$ state has a long lifetime, several hundred microseconds. However, its effective lifetime in this experiment is much shorter, on the order of 10 $\mu$s. This is due to two considerations. First, as described by Eq. (20) of Sec. II, the volume containing the excited-state atoms expands after the laser pulse (since the atoms have a wide range of velocities in the effusive beam), thus lowering the excited-state density and therefore the excited-state–excited-state collision probability significantly on a time scale of about 5 $\mu$s. Second, most of the atoms will have moved out of the region imaged by the lens after 10–20 $\mu$s.

In order to confirm that the observed final-state fluorescence is emitted only at 423 nm, the lens and interference filter optical system was replaced with an optical fiber that transmits the fluorescence to a monochromator. As the monochromator is scanned, the fluorescence shows up as a peak centered at about 420 nm. The slits on the monochromator were set as wide open as possible, 6 mm, in order to observe the weak 423-nm fluorescence. This gives a bandwidth for the monochromator of 24 nm. However, the Ca is only excited to its lowest-energy levels, so there should be no nearby emissions. The only other strong fluorescence observed with the monochromator is the 657-nm emission from the laser-prepared Ca($4s4p\ ^3P_1$), which decays to the ground state. The possibility of fluorescence near 612 nm from the $4s5s\ ^3S_1 \rightarrow 4s4p\ ^3P_1$ transition was investigated but not observed. This would indicate energy pooling to the $4s5s\ ^3S_1$ state. Also, we did not look in the infrared for the 1.03-$\mu$m emission from the $4s5s\ ^1S_0 \rightarrow 4s4p\ ^1P_1$ transition, which would be indicative that the $4s5s\ ^1S_0$ state is populated by energy pooling.

The signal strength observed from the final state ranges from one photon every 5 or 10 ns down to slightly more than

one photon every 1 $\mu$s. For fluorescence intensities at the high end of this range, the output of the PMT's preamplifier is taken directly into a 125-MHz digital oscilloscope. The digital oscilloscope was also used to record the initial-state fluorescence. For lower strength final-state signals, the PMT is used in pulse counting mode and the data are recorded with a multichannel scaler with a bin width of 5 ns. Each final-state data set represents an average $10^5$ pulses coadded and each initial-state data set represents an average of several thousand laser pulses.

Before analyzing the data, the background is subtracted. When the oscilloscope is used, this background is determined by averaging the voltage over a period of 1 $\mu$s taken before the laser pulse. When the multichannel scaler is used, the average signal between 30 and 40 $\mu$s after the laser pulse is used for the background. This is when all of the energy pooling signal has died away. Between 0 and 0.8 $\mu$s after the laser pulse, there is some additional background due to scattered laser light and electrical noise. In some of the figures presented, the data are plotted with this background subtracted off as well. However, when the alignment parameters are extracted, the data taken between 0 and 1 $\mu$s after the laser pulse are not used.

## IV. EXPERIMENTAL RESULTS

The magnetic precession can be easily observed in the fluorescence of the initially excited $4s4p\ ^3P_1$ state. For example, when linear polarization is used, no fluorescence is emitted from the initial state in a direction parallel to the symmetry axis, and the maximum fluorescence intensity is emitted perpendicular to the symmetry axis. If the $4s4p\ ^3P_1$ atoms precess so that the symmetry vector points first towards and then away from the detector, a modulation is seen in the observed $4s4p\ ^3P_1 \rightarrow 4s^2\ ^1S_0$ fluorescence. This is illustrated in Figs. 5(a) and 5(b), where the 657-nm fluorescence intensity as a function of time is plotted. In Fig. 5(a) the excitation laser is linearly polarized parallel to the **z** axis and the magnetic field is directed along the **x** axis. Little modulation is seen because as the orbital precesses, the symmetry vector remains perpendicular to the **x** axis. The small amount of modulation that is present is due to the fact that neither the magnetic field nor the detector is perfectly aligned along the **x** axis. In Fig. 5(b), on the other hand, the excitation laser is polarized parallel to the **x** axis and the magnetic field is directed along the **z** axis. The symmetry vector now rotates from pointing toward the detector to perpendicular to it, resulting in a large modulation in the observed signal. The reason for the long-term rise and fall is that the laser is positioned slightly upstream of the observation region. The velocity of the beam brings the excited atoms directly in front of and then past the detector.

The effects of this precession are also seen in the modulated final-state signal since the energy pooling cross section depends on the orbital alignment [as predicted by Eq. (13)]. Here both fourfold and twofold contributions to the signal occur. This modulation, with a period of 0.4 $\mu$s is shown in Fig. 6(a) for both linear and circular polarization, where the 423-nm fluorescence intensity is plotted as a function of time. In the linear case the laser is polarized parallel to the **z** axis and in the circular case it is polarized around the **y** axis.

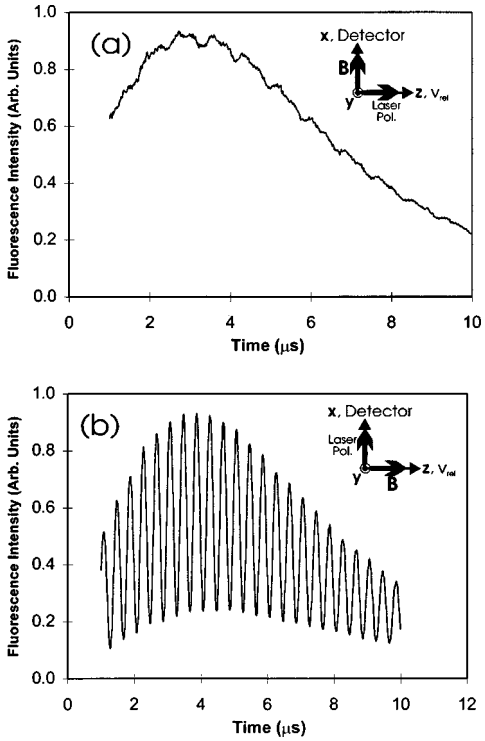


FIG. 5. Typical fluorescence signals from the initial $4s4p\ ^3P_1$ state plotted as a function of time, showing the magnetic precession of the initially excited state. (a) The magnetic field is directed along the **x** axis and the excitation laser is polarized parallel to the **z** axis. Because the detector is slightly off axis and the magnetic field is not perfectly aligned with the **z** axis, some modulation is seen. The laser is positioned slightly upstream of the area imaged by the lens, so the signal peaks and then drops off as the velocity of the beam brings the excited atoms past the detector. (b) The magnetic field is directed along the **z** axis and the excitation laser is polarized parallel to the **x** axis. Because the fluorescence is emitted anisotropically as the $4s4p\ ^3P_1$ state decays to the ground state and the atoms are precessing around an axis perpendicular to the direction from the excited atoms to the detector, large modulations are seen in the observed final-state fluorescence.

In both cases, the magnetic field points in the **x** direction; perpendicular to both the beam axis and the symmetry vector of the orbital. The geometry of the linear case is the same as the initial-state signal shown in Fig. 5(a). The reason large modulations are seen in the final state and not in the initial state is that in Fig. 6(a) the energy pooling cross section depends on the angle between the symmetry vector and the **z** axis instead of the angle between the symmetry vector and the **x** axis. The fluorescence intensity is expressed here in arbitrary units and the signal will be normalized later, when the long-term rise and fall is quantified relative to the modulations due to the precession.

As shown in Fig. 6(a), the final-state signal from the linearly polarized case is much larger than the circularly polarized case. In order to accurately measure this, the magnetic field was directed along the **z** axis and the laser was linearly polarized in the **x** direction. A $\frac{1}{4}$-wave plate was placed in front of the polarizer. Ten sets of 1000 laser pulses each were alternately recorded, either with the axis of the $\frac{1}{4}$-wave plate aligned with the **x** axis, leaving the light linearly polarized along the **x** axis, or with the axis of the $\frac{1}{4}$-wave plate rotated

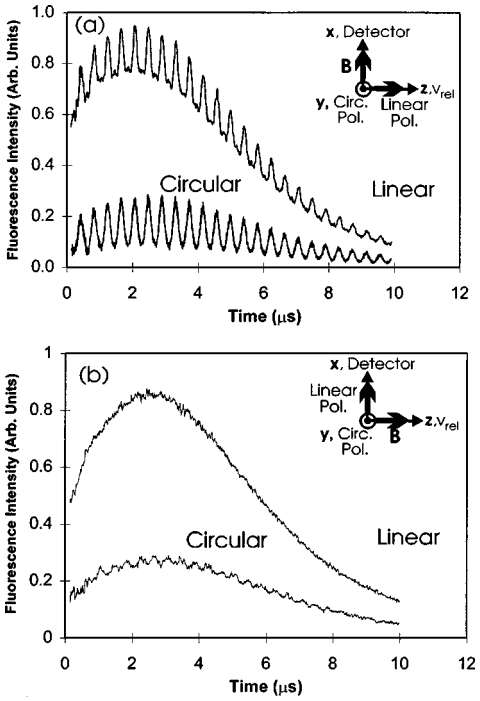


FIG. 6. Typical fluorescence signals from the final $4s4p\ ^1P_1$ state excited with linear polarization plotted as a function of time. (a) For the upper curve, the initial state is excited with linearly polarized light, while in the lower curve it is excited with circularly polarized light. The magnetic field is directed in the **x** direction, perpendicular to both the beam axis and the symmetry vector of the orbital. The modulation $I(t)=a\cos(2\beta)+b\cos(4\beta)+c$, where $\beta=\omega t+\beta_0$, is clearly visible in both curves on top of a much slower amplitude change in the signal. For the case of linear polarization the signal is greatest when $\beta=0$, while for the case of circular polarization it is greatest when $\beta=90°$. Note that in the linear case the laser polarization is parallel to the **z** axis, so for this curve $\beta_0=0$. However, for the circular case $\beta_0=90°$ since the laser always propagates in the **y** direction. (b) Data similar to the data in (a), except now the magnetic field is directed along the **z** axis. In the case of linear polarization, the laser is polarized along the **x** axis, while in the case of circular polarization, the laser is again propagating along the **y** axis. This results in $\beta=90°$ at all times for both the linear and circular polarization cases, so there is little modulation in the signal. The small modulation that is present is probably due to a misalignment in the direction of the magnetic field with respect to the beam axis. These modulations represent an upper limit on the anisotropy in the emission of final-state fluorescence around the **z** axis.

45° to the **x** axis, producing circularly polarized light. In this geometry, the orbitals precess around the **z** axis, always maintaining $\beta=90°$. Thus we find that the ratio of the circular to linear cross section at $\beta=90°$, $r$, is $0.36\pm0.01$ near $t=0$. The linear and circular data shown in Fig. 6(a) were taken on different days and rescaled for this figure to approximately reflect the actual value of $r$.

The slow rise and fall in Fig. 6(a) is in part due to the motion of the excited atoms past the detector, as in the initial-state signals of Fig. 5. However, there is an additional contribution to the long-term decay in the final-state signal due to the decrease in frequency of the higher-velocity collisions, as described previously. The decay in Fig. 6 is visibly faster than the decay in Fig. 5.

In the case of linear polarization, the cross section is greatest when $\beta=0$, i.e., when the $m_j=0$ substrate is populated. At $\beta=90°$ a superposition of the $m_j=1$ and $-1$ states are populated. In the case of circular polarization it is greatest when $\beta=90°$. Here a superposition of all three magnetic substates is populated. The minimum for circular polarization occurs at $\beta=0$ when only the $m_j=1$ (or only $m_j=-1$) states are populated. Note that for the case of linear polarization, the laser polarization is parallel to the **z** axis, so that $\beta_0=0$. For the case of circular polarization, $\beta_0=90°$.

In the linear case, the modulation has an amplitude of nearly 20% of the mean signal strength and is obviously not a simple cosine curve. As shown below, a $\cos(2\beta)$ term plus a smaller $\cos(4\beta)$ term fits this shape very well. The oscillations in the circular case are a much larger fraction of the total signal. Here the minimum signal is 60% smaller than the maximum. A small $\cos(4\beta)$ term is also needed to accurately fit this curve. Before this fitting procedure is described, several details are considered.

There is the possibility that the final state may be aligned relative to the initial state. If this were the case, some of the modulation in the final-state signal of Fig. 6(a) may be due to the anisotropic emission of fluorescence from the final state. It is possible to show, however, that this is not the case here. Consider the final $4s4p\ ^1P_1$ state in terms of the chemical basis of $p_x$, $p_y$, and $p_z$ states. The PMT is located in the **x** direction from the interaction region; it detects fluorescence equally well from the $p_y$ and $p_z$ states, but collects little light from the $p_x$ state. Figure 6(b) shows final-state fluorescence data similar to that in Fig. 5(a), except now the magnetic field is directed along the **z** axis. In the case of linear polarization the laser is now polarized along the **x** axis, while in the case of circular polarization the laser is again polarized around the **y** axis. In this geometry the orbitals precess about the **z** axis always keeping $\beta=90°$. Any azimuthal anisotropy in the final-state fluorescence around the **z** axis should be visible as oscillations in the signal. However, no large oscillations are seen. The small oscillations in Fig. 6(b) are most likely a result of misalignments in the magnetic field with respect to the **z** axis. These oscillations represent an upper limit for the difference in the $p_x$ and $p_y$ final-state populations. The amplitude relative to the total signals for these oscillations is less than 0.01 for the linear polarization case and 0.05 for the circular case. The mean free path of photons emitted at the 423-nm resonance, given the calcium density in this experiment, is 5 cm, indicating that photon scattering, which would obscure any anisotropies in the fluorescence, should also have a minimal effect.

Although we have shown that there is a negligible difference in the $p_x$ and $p_y$ final-state populations, there may still be a difference in the $p_y$ and $p_z$ populations. Thus the ratio of undetected to detected fluorescence $p_x/(p_y+p_z)$ could change. Further work indicates that this effect is small [25].

Although most of the fluorescence at 423 nm is a result of the energy pooling process $4s4p\ ^3P_1+4s4p\ ^3P_1\rightarrow 4s^2\ ^1S_0+4s4p\ ^1P_1$, it is possible that the $4s4p\ ^1P_1$ state could also be populated by an additional path of energy pooling to the $4s5s\ ^1S_0$ state, followed by its decay to the $4s4p\ ^1P_1$ state. However, this process, $4s4p\ ^3P_1+4s4p\ ^3P_1\rightarrow 4s^2\ ^1S_0+4s5s\ ^1S_0$, is endothermic by

2900 $cm^{-1}$ and thus will occur only for collisions with sufficient energy, in the tail of the beam velocity distribution. The minimum relative velocity required is 1300 m/s. For the data shown in Fig. 6, the width of the laser beam in the **z** direction is 3 mm. This means that most of the collisions with a relative velocity of at least 1300 m/s occur within the first microsecond after the laser pulse and none of these collisions occur at all after 2.3 $\mu$s. The lifetime of the $4s5s\ ^1S_0$ state is about 50 ns [26], so any cascade fluorescence will be observed immediately after the collision occurs. Since there is no abrupt increase in fluorescence in the first several microseconds after the laser pulse and the alignment effect does not change abruptly at these early times, we conclude that any signal from cascade fluorescence from the $4s5s\ ^1S_0$ level is not observable in this experiment. It may, at first, seem surprising that energy pooling to the $4s4p\ ^1P_1$ level, which is exothermic by 6800 $cm^{-1}$, occurs and energy pooling to the $4s5s\ ^1S_0$ level, which is endothermic by only 2900 $cm^{-1}$, does not happen. However, experiments with Sr (which is very similar to Ca) have shown that the rate constant for energy pooling from the Sr($5s5p\ ^3P_1$) state to the Sr($5s6s\ ^1S_0$) level at 700 K is only 1% of the rate constant to the Sr($5s5p\ ^1P_1$) level [17]. Although these rate constants are for a slightly lower temperature than our experiment was carried out at, this is more than made up for by the fact that the 2900 $cm^{-1}$ energy defect for energy pooling to the Ca($4s5s\ ^1S_0$) level is almost twice that for the corresponding process in Sr.

The 2-MHz oscillations in the final $4s4p\ ^1P_1$ state fluorescence of Fig. 6(a) therefore represent the modulations in the energy pooling cross section due to the magnetic precession. In order to quantitatively describe this modulation, we must also quantify the long-term rise and decay. This is done by dividing each point in Fig. 4(a) by a running average taken over one period (in $\beta$) around that point. The result is shown in Fig. 7 for both the linear and circular cases (note the ordinate scales). The data are now normalized so that each signal has a value of 1 when the oscillations are averaged out. This means that the parameters $a_l'$, $b_l'$, $a_c'$, and $b_c'$, which are the relative amplitudes of the oscillations with respect to the mean signal [defined in Eq. (15) of Sec. II], are simply the amplitudes of the cos(4$\beta$) and cos(2$\beta$) terms in Fig. 7. In order to show that the data do fit this form, the average signal for one full precession period and the corresponding fit is plotted in Fig. 8. However, since the fit parameters do change over time, the fit parameters obtained directly from Fig. 8 do not have a straightforward interpretation.

Instead, we first restrict our attention to the first several microseconds after the laser pulse. Recall that [by Eq. (20)] the signal at late times represents only low-velocity collisions, while at early times the data more properly represent the cross sections averaged over the thermal velocity distribution of the beam. In addition, small fluctuations in the magnetic field due to nearby electrical equipment tend to smear out the alignment effect at later times. The first column of Table I gives the fitted values of the parameters $a_l'$, $b_l'$, $a_c'$, and $b_c'$ averaged over the first five oscillations in Fig. 6. The parameter $r$, which is the ratio of the circularly polarized final-state signal to the linearly polarized final-state signal at $\beta = 90°$ [defined in Eq. (16) of Sec. II], is also given here, averaged over the same times as the other parameters. The velocity distribution of the colliding atoms has a mean of 780 m/s and a FWHM of 810 m/s at the start of this time

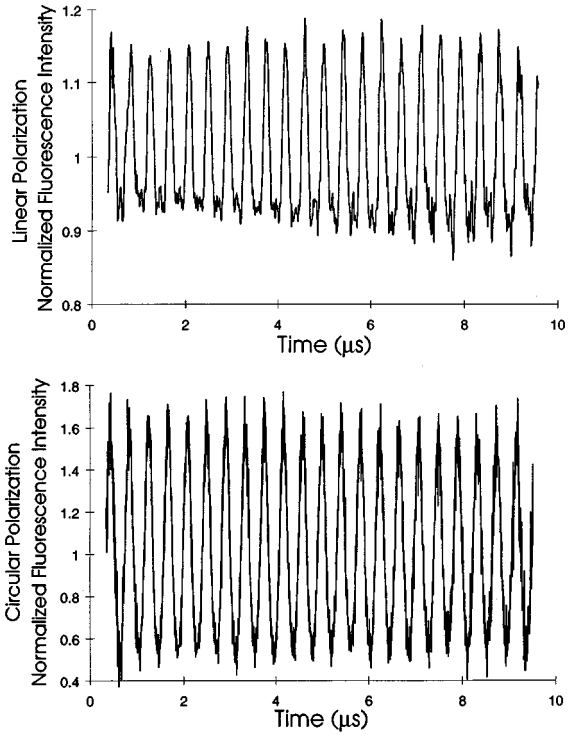


FIG. 7. Data in Fig. 6(a) displayed with the long-term rise and fall normalized out. This is done by dividing each point in Fig. 6(a) by a running average equal to one oscillation period. Each signal is now normalized so that the mean signal value is one. The parameters $a_l'$, $b_l'$, $a_c'$, and $b_c'$ are simply the amplitudes of the cos(2$\beta$) and cos(4$\beta$) components of each curve in this figure.

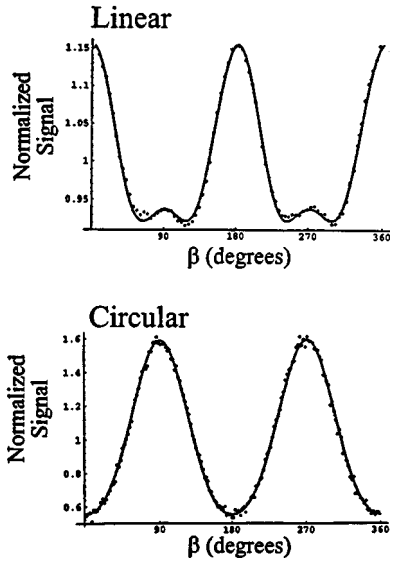


FIG. 8. Data from Fig. 7 have been divided into sections, each one full precession period long, and all of the sections are averaged together. This average precession period signal (dots) along with the fit to the form $a\ \cos(2\beta)+b\ \cos(4\beta)+1$ (solid line) is plotted for both the linear and circular cases. The data fit this form very well.

TABLE I. Values of the parameters $a_l'$, $b_l'$, $a_c'$, $b_c'$, and $r$.

| Parameter | Relative value for initial velocity distribution[a] | Trend[b] |
|---|---|---|
| $a_l'$ | $0.096^{+0.009}_{-0.004}$ | $+0.6\pm0.1$ |
| $b_l'$ | $0.043^{+0.008}_{-0.004}$ | $+1.0\pm0.3$ |
| $a_c'$ | $-0.53^{+0.01}_{-0.02}$ | $-0.16\pm0.04$ |
| $b_c'$ | $0.071^{+0.013}_{-0.006}$ | $+0.4\pm0.2$ |
| $r$ | $2.78\pm0.07$ | $-0.20\pm0.05$ |

[a]The average values from the data between 1 and 2.7 $\mu$s. During this time period the values of the parameters are fairly constant. The velocity distribution of the colliding atoms has a mean of 780 m/s and a FWHM of 810 m/s at the start of this time period and a mean of 600 m/s and a FWHM of 680 m/s at the end.

[b]The fractional change between the values in the first column and the values at 7.7 $\mu$s, when the velocity distribution has a mean of 190 m/s and a FWHM of 210 m/s.

period and a mean of 600 m/s and a FWHM of 680 m/s at the end.

When the parameters are calculated as a function of time, the effects of the velocity dependence of the parameters and the smearing out due to nonuniform magnetic fields causes the values to shift by less than 10% over the time period of the first several microseconds. In addition to this uncertainty, there is an uncertainty due to statistical noise. The statistical error is about 4% for $a_l$, 6% for $b_l$, 1% for $a_c$, and 10% for $b_c$. Finally, there is error because the magnetic field and the laser polarizations may not be exactly perpendicular to the atomic beam axis. There is an uncertainty of $\pm10°$ for alignment of the magnetic field and $\pm5°$ for the alignment of the laser polarization. The effect of these misalignments is to make the measured values lower than the actual values. The values given in this paper underestimate the true values of $b_l$ and $b_c$ by up to 10%, $a_l$ by up to 5%, and $a_c$ by up to 4%.

The fundamental cross sections can now be calculated with Eq. (19). They are given in the first column of Table II.

TABLE II. Values of the fundamental cross sections calculated using Eq. (19).

| Fundamental cross section | Relative value for initial velocity distribution[a] | Trend[b] |
|---|---|---|
| $\sigma_{00}$ | $1.14^{+0.02}_{-0.01}$ | $+0.090$ |
| $\sigma_{11}$ | $0.11^{+0.02}_{-0.02}$ | $0\pm0.1$ |
| $\sigma_{1-1}+\sigma_{1-1;-11}$ | $1.80^{+0.05}_{-0.09}$ | $-0.03\pm0.01$ |
| $\sigma_{01}+\sigma_{01;10}$ | $0.24^{+0.02}_{-0.04}$ | $0\pm0.08$ |
| $\mathrm{Re}(\sigma_{00;1-1})$ | $-0.61^{+0.03}_{-0.02}$ | $+0.20$ |

[a]Values calculated from column 2 in Table I. These are the average values when the velocity distribution of the colliding atoms ranges from a mean of 780 m/s and a FWHM of 810 m/s to a mean of 600 m/s and a FWHM of 680 m/s. These values are normalized to $\frac{1}{8}(3\sigma_{00}+\frac{3}{2}\sigma_{11}+\frac{3}{2}\sigma_{1-1}+\frac{3}{2}\sigma_{1-1;-11}+2\sigma_{01}+2\sigma_{01;10}-2\ \mathrm{Re}\ \sigma_{00;1-1})=1$.

[b]Relative change in the cross sections as the velocity distribution goes from that of column 2 to a mean of 190 m/s and a FWHM of 210 m/s.

The dominant cross sections are $\sigma_{00}$, $\sigma_{1-1}+\sigma_{1-1;-11}$, and $\mathrm{Re}\ \sigma_{00;1-1}$. The cross sections $\sigma_{11}$ and $\sigma_{01}+\sigma_{01;10}$ are small. This is why the energy pooling signal decreases so much when circular polarization is used. When $\beta=0°$ with circular polarization, both colliding atoms are in the $m_j=1$ state. The observed cross section is proportional to $\sigma_{11}$, the smallest of all the cross sections. When circular polarization is used and $\beta=90°$, the atoms are in a superposition of all magnetic sublevels and the observed signal is

$$I_c(90°)\propto\tfrac{1}{8}\sigma_{11}+\tfrac{1}{4}\sigma_{00}+\tfrac{1}{8}(\sigma_{1-1}+\sigma_{1-1;-11})+\tfrac{1}{2}(\sigma_{01}+\sigma_{01;10})+\tfrac{1}{2}\ \mathrm{Re}\ \sigma_{00;1-1}. \quad (24)$$

In this case the system is in a superposition of states that have larger energy pooling cross sections. The fact that $\mathrm{Re}\ \sigma_{00;1-1}$ is negative makes the signal with circular polarization lower than the signal with linear polarization. For example, the signal at $\beta=45°$ with linear polarization is proportional to

$$I_l(45°)\propto\tfrac{1}{8}\sigma_{11}+\tfrac{1}{4}\sigma_{00}+\tfrac{1}{8}(\sigma_{1-1}+\sigma_{1-1;-11})+\tfrac{1}{2}(\sigma_{01}+\sigma_{01;10})-\tfrac{1}{2}\ \mathrm{Re}\ \sigma_{00;1-1}. \quad (25)$$

This is the same as Eq. (23), except the signal is increased because the value of $\mathrm{Re}\ \sigma_{00;1-1}$ is negative.

Finally, the behavior of the alignment effect as a function of time can be considered. Notice, in Fig. 7, that the amplitude of the oscillation for the linear polarization case increases slightly over time. This is due to the velocity dependence of the cross sections. The signal at later times corresponds to lower-energy collisions. This effect is even larger than seen in Fig. 7. The magnetic fields in the interaction region fluctuate slightly, causing the average orbital alignment to smear out at late times. These fluctuations are caused by nearby electrical equipment, primarily the large roughing pump attached to the vacuum chamber and have an amplitude on the order of 0.01 G and a frequency on the order of 100 Hz. The exact amount of smearing is quantified from the oscillation data for the initial-state fluorescence. The amplitude of the initial-state oscillations decreases linearly in time at a rate of $0.031\pm0.005$ times the initial amplitude per microsecond. These initial-state oscillations have a period of $2\beta$, so the observed values of the $a_l'$ and $a_c'$ final-state fit parameters will decrease (with respect to their true values) due to dephasing at the same rate. The $4\beta$ parameters $b_l'$ and $b_c'$ will decrease at twice this rate. The parameter $r$ is not affected by the dephasing. The magnetic field must fluctuate by 3% of its total value or by about 0.006 G to cause this dephasing.

Instead of averaging over several oscillations in Fig. 7, each oscillation is fit individually to determine the parameters $a_l'$, $b_l'$, $a_c'$, and $b_c'$ as a function of time. As an illustrative example, Fig. 9 shows the values of $a_l'$ up to a time of 8 $\mu$s. Plotted here are the values both before and after correcting for the dephasing due to magnetic-field fluctuations. In both cases, the values clearly increase with increasing time. Because of the dephasing and because the time scale cannot be precisely related to velocity, we cannot give an exact form for the velocity dependence of this parameter. We can state that $a_l'$ increases by a factor of $1.5\pm0.2$ as the

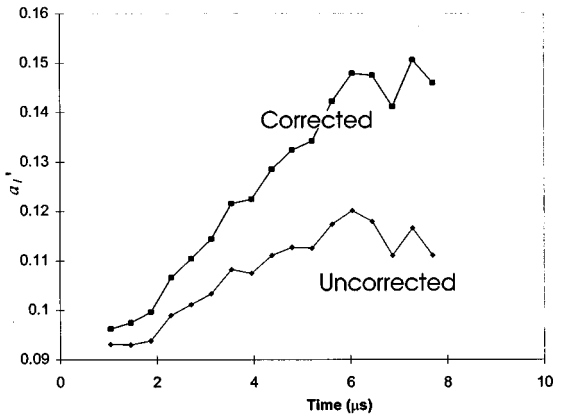


FIG. 9. For illustrative purposes, the parameter $a_l'$ is plotted as a function of time. The uncorrected curve shows the actual amplitudes of the linear $\cos(2\beta)$ component in Fig. 7. The other curve includes the dephasing correction. Both curves show a definite increasing trend with time, although the trend in the corrected curve is about twice that in the uncorrected curve. Since there is a substantial uncertainty in the dephasing correction and the time axis cannot be exactly related to the collision velocity, the most that can be concluded from these data is that the value of $a_l'$ increases by approximately 60% as the collision velocity decreases from a mean of 800 m/s to a mean of about 190 m/s.

collision velocity decreases from a mean of 800 m/s to a mean of about 190 m/s. This, along with the trend in velocity dependence for the other measured quantities, is shown in the last column of Table I. The value of $b_l'$, although small, almost doubles as the collision velocity drops from 800 to 190 m/s. The alignment effect in the circular case also increases with decreasing velocity. The magnitude of both $a_c'$ and $b_c'$ increases by about 20% over the measured velocity range (the value of $a_c'$ decreases, but since it is negative this increases its magnitude). The trends resulting from the changes in the fundamental cross sections are shown in the final column of Table II.

## V. CONCLUSION

A complete explanation of these alignment results will require all of the relevant Ca-Ca potentials, which are not yet available. However, a few comments can still be made. The smallest cross section is $\sigma_{11}$. If two atoms in the $m_j=1$ state collide with a relatively small impact parameter, the system has a total electronic angular momentum around the internuclear axis of $\Omega=2$. If the coriolis coupling is small, $\Omega$ is approximately conserved. Thus the system will not be able to transfer to the final $\mathrm{Ca}(4s4p\ ^1P_1)+\mathrm{Ca}(4s^2)$ state, which must have $\Omega=0$ or 1. Since the sum $\sigma_{10}+\sigma_{10;01}$ has the next smallest value, it is tempting to consider that only $\Omega=0$ states are involved in the energy pooling. However, calculations for the analogous Sr system show that there is a strong avoided crossing between the $^1\Pi_u$ potential-energy curves correlating to the $\mathrm{Sr}(5s5p\ ^3P)+\mathrm{Sr}(5s5p\ ^3P)$ and the $\mathrm{Sr}(5s5p\ ^1P)+\mathrm{Sr}(5s^2)$ asymptotic states [27]. There is likely a similar situation with Ca since the properties of these two elements are very close.

The sudden locking approximation is often used to calculate polarization effects in collisions, such as in $\mathrm{Na}(3p)+\mathrm{Na}(3p)$ associative ionization [21,28,29]. In this approximation the atoms are treated as noninteracting when they are separated by greater than the locking radius, and the total angular momentum of each atom $j$ and its projection along the laboratory fixed $\mathbf{z}$ axis $m_j$ are conserved. At the locking radius, these $|j_1,m_1;j_2,m_2\rangle$ states are projected on the molecular states $|^{2S+1}\Lambda_{g/u}\rangle$ and $S$, $\Lambda$, and parity are taken to be the conserved quantities inside the locking radius.

As a first crude step, this approximation can be applied to the $\mathrm{Ca}(4s4p\ ^3P_1)+\mathrm{Ca}(4s4p\ ^3P_1)$ collision. Decomposing the $|j,m_j\rangle$ states into $|l=1,m_l,s=1,m_s\rangle$ states,

$$|j=1,m_j=0\rangle=\frac{1}{\sqrt{2}}\left(|m_l=1,m_s=-1\rangle - |m_l=-1,m_s=1\rangle\right),$$
$$|j=1,m_j=1\rangle=\frac{1}{\sqrt{2}}\left(|m_l=1,m_s=0\rangle - |m_l=0,m_s=1\rangle\right). \tag{26}$$

For low impact parameter collisions, $\Lambda$ is approximately the sum of $m_l$ over both atoms and spin must still be added as a vector. For two $m_j=0$ states colliding, half of the wave function ends up in $^5\Delta$ states ($|m_l-1,m_s=-1\rangle$ colliding with $|m_l=1,m_s=-1\rangle$, for example) and the other half in $^{5,1}\Sigma$ states ($|m_l=1,m_s=-1\rangle$ colliding with $|m_l=1,m_s=1\rangle$, for example, where $^{5,1}\Sigma$ indicates a sum of both $^1\Sigma$ and $^5\Sigma$ states). The part of the wave function that is in the $^5\Delta$ states will find it difficult to get to the final $\mathrm{Ca}(4s4p\ ^1P_1)+\mathrm{Ca}(4s^2)$ state, which must be either $^1\Sigma$ or $^1\Pi$. When an $m_j=1$ state collides with an $m_j=-1$ state, the same $^1\Sigma$ states are populated, but instead of the $^5\Delta$ states, $^{5,3}\Pi$ states are populated. These $^{5,3}\Pi$ states may have a greater chance of being transferred to the final $^1\Sigma$ or $^1\Pi$ states through spin-orbit or coriolis coupling. This could explain why the cross section $\sigma_{1-1}+\sigma_{1-1;-11}$ is larger than $\sigma_{00}$. Similarly, when an $m_j=0$ state collides with an $m_j=1$ state no $^1\Sigma$ states are populated and half the wave function ends up in $^5\Pi$ or $^{5,3}\Delta$ states, which may not be able to get to the final states. The other half of the wave function goes to $^{5,1}\Pi$ and $^{5,3}\Sigma$ states and these may also find it hard to get to the $^1\Sigma$ or $^1\Pi$ final states, explaining why $\sigma_{10}+\sigma_{10;01}$ is small. However, it is not immediately easy to reconcile why the $^{5,1}\Pi$ and $^{5,3}\Sigma$ states cannot get to the final state, but the $^{5,3}\Pi$ states that occur in an $m_j=1$ plus an $m_j=-1$ collision can. Also, this preliminary analysis cannot say anything about the values of the coherence cross sections.

These remarks are meant only to be a first comment on the data obtained by this experiment. The sudden locking approximation must be viewed with great suspicion when applied to this situation since the spin-orbit precession rate is actually much shorter than the collision time. There is probably ample time for the angular momentum to be altered during the transition from the region where the $j$ and $m_j$ of each atom is conserved to the region where molecular $\Lambda$, $S$, and parity are conserved. Although the behavior in this re-

gion is complicated, the fact that such large polarization effects are observed indicates that important general principles are waiting to be uncovered by a careful theoretical analysis of this system.

In this paper we have shown that we can almost completely describe the magnetic sublevel dependence of the $Ca(4s4p\ ^3P_1)+Ca(4s4p\ ^3P_1)\rightarrow Ca(4s4p\ ^1P_1)+Ca(4s^2)$ energy pooling process. Very large differences in these fundamental cross section are found, with $\sigma_{00}$, $\sigma_{1-1}+\sigma_{1-1;-11}$, and the interference term $\mathrm{Re}(\sigma_{00;1-1})$ dominating the observed signal. Moreover, the energy dependence of these parameters is determined. This experiment also introduces a technique where precession in a magnetic field is used to control the alignment of the orbitals. We note that this technique is only applicable to collision processes where there is a long-lived initial state and a quickly decaying final state. In future experiments the polarization of the final-state fluorescence will be characterized in order to determine the final-state alignment [25]. In addition, it is possible to extract cross sections that we were unable to measure in this experiment using either two excitation lasers or magnetic-field gradients [25].

## ACKNOWLEDGMENT

The authors gratefully acknowledge the support of the National Science Foundation.

[1] I. V. Hertel, H. Schmidt, A. Bahring, and E. Meyers, Rep. Prog. Phys. **48**, 375 (1985).
[2] E. E. B. Campell and I. V. Hertel, Adv. Chem. Phys. **72**, 37 (1988).
[3] S. R. Leone, Acc. Chem. Res. **25**, 71 (1992).
[4] L. Kovalenko, in *The Chemical Dynamics and Kinetics of Small Radicals*, edited by K. Liu and A. Wagner (World Scientific, Singapore, 1995), p. 730.
[5] R. A. Lasell, B. S. Bayram, and M. D. Harvey, Phys. Rev. A **56**, 2095 (1997).
[6] E. M. Spain, M. J. Dalberth, P. D. Kleiber, and S. R. Leone, J. Chem. Phys. **102**, 9532 (1995).
[7] W. Bussert, D. Neuschafer, and S. R. Leone, J. Chem. Phys. **87**, 3833 (1987).
[8] C. J. Smith, J. P. J. Driessen, L. Eno, and S. R. Leone, J. Chem. Phys. **96**, 8212 (1992).
[9] J. P. J. Driessen and L. Eno, J. Chem. Phys. **97**, 5532 (1992).
[10] E. E. B. Campbell, H. Husler, R. Witte, and I. V. Hertel, Z. Phys. D **16**, 21 (1990).
[11] S. S. Op de Beek, J. P. J. Driessen, K. H. J. M. Robben, H. C. W. Beijerinck, and B. J. Verhaar, Phys. Rev. A **56**, 2833 (1997).
[12] H. A. J. Meijer, T. J. C. Pelgrim, H. G. M. Heideman, R. Morgenstern, and N. Andersen, Phys. Rev. Lett. **59**, 2939 (1987); J. Chem. Phys. **90**, 738 (1989).
[13] J. G. Kircz, R. Morgenstern, and G. Nienhuis, Phys. Rev. Lett. **48**, 610 (1982).
[14] M.-X. Wang, J. Keller, J. Boulmer, and J. Weiner, Phys. Rev. A **35**, 934 (1987).
[15] J. H. Nijland, J. A. de Gouw, H. A. Dijkerman, and H. G. M. Heideman, J. Phys. B **25**, 2841 (1992).
[16] J. F. Kelly, M. Harris, and A. Gallagher, Phys. Rev. A **38**, 1225 (1988).
[17] J. A. Neuman, J. Cooper, and A. Gallagher, Phys. Rev. A **56**, 432 (1997).
[18] J. A. Neuman, A. Gallagher, and J. Cooper, Phys. Rev. A **50**, 1292 (1994).
[19] J. A. Neuman and A. Gallagher, Phys. Rev. A (to be published).
[20] G. Gabbanini, A. Lucchesini, and S. Gozzini, J. Phys. B **27**, 4643 (1994); A. Obrebski, R. Hergenroder, and K. Niemax, Z. Phys. D **14**, 289 (1989).
[21] D. Husain and G. Roberts, J. Chem. Soc., Faraday Trans. 2 **82**, 1921 (1986).
[22] D. M. Jones and J. S. Dahler, Phys. Rev. A **35**, 3688 (1986).
[23] H. A. J. Meijer *et al.*, J. Chem. Phys. **90**, 729 (1989).
[24] J. P. J. Driessen and S. R. Leone, J. Phys. Chem. **96**, 6136 (1992).
[25] H. Parks and S. Leone (unpublished).
[26] J. Mitroy, J. Phys. B **26**, 3703 (1993).
[27] N. Boutassetta, A. R. Allouche, and M. Auber-Frecon, Phys. Rev. A **53**, 3845 (1996).
[28] B. Huynh, O. Dulieu, and F. Masnou-Seews, Phys. Rev. A **57**, 958 (1998).
[29] I. Y. Yurova, J. Phys. B **28**, 999 (1995).